Title

Inferring single-cell behaviour from large-scale epithelial sheet migration patterns.

Journal

Journal of the Royal Society. Interface, 14(130)

Authors

Lee, Rachel

Yue, Haicen

Rappel, Wouter-Jan

et al.

Publication Date

2017-05-01

DOI

10.1098/rsif.2017.0147

Peer reviewed

INTERFACE

rsif.royalsocietypublishing.org

Research

Cite this article: Lee RM, Yue H, Rappel W-J, Losert W. 2017 Inferring single-cell behaviour from large-scale epithelial sheet migration patterns. *J. R. Soc. Interface* **14**: 20170147. http://dx.doi.org/10.1098/rsif.2017.0147

Received: 28 February 2017
Accepted: 13 April 2017

Subject Category:
Life Sciences–Physics interface

Subject Areas:
biophysics

Keywords:
collective migration, epithelial cells, modelling

Authors for correspondence:
Rachel M. Lee
e-mail: rmlee@umd.edu
Wolfgang Losert
e-mail: wlosert@umd.edu

Electronic supplementary material is available online at https://dx.doi.org/10.6084/m9.figshare.c.3757265.

THE ROYAL SOCIETY PUBLISHING

Inferring single-cell behaviour from large-scale epithelial sheet migration patterns

Rachel M. Lee[1], Haicen Yue[2], Wouter-Jan Rappel[2] and Wolfgang Losert[1]

[1]Department of Physics, University of Maryland, College Park, MD, USA
[2]Department of Physics, University of California, San Diego, CA, USA

RML, 0000-0001-9359-0422

Cell migration plays an important role in a wide variety of biological processes and can incorporate both individual cell motion and collective behaviour. The emergent properties of collective migration are receiving increasing attention as collective motion's role in diseases such as metastatic cancer becomes clear. Yet, how individual cell behaviour influences large-scale, multi-cell collective motion remains unclear. In this study, we provide insight into the mechanisms behind collective migration by studying cell migration in a spreading monolayer of epithelial MCF10A cells. We quantify migration using particle image velocimetry and find that cell groups have features of motion that span multiple length scales. Comparing our experimental results to a model of collective cell migration, we find that cell migration within the monolayer can be affected in qualitatively different ways by cell motion at the boundary, yet it is not necessary to introduce leader cells at the boundary or specify other large-scale features to recapitulate this large-scale phenotype in simulations. Instead, in our model, collective motion can be enhanced by increasing the overall activity of the cells or by giving the cells a stronger coupling between their motion and polarity. This suggests that investigating the activity and polarity persistence of individual cells will add insight into the collective migration phenotypes observed during development and disease.

1. Introduction

Collective cell migration is an important biological phenotype used in many biomedical assays. For example, in a wound healing assay, the speed at which two monolayers of cells migrate towards each other is often measured to determine a cell migration response to drug treatments. The use of collective migration as a biomedical phenotype stems from its important role in many biological processes; collective migration is essential for development [1,2] and wound healing [3,4], but its misregulation plays a role in diseases such as metastatic cancer [5,6]. It is non-trivial, however, to infer single-cell migration behaviours from metrics such as the monolayer boundary displacement. Despite many studies on the behaviour of individual cells, which have looked at features of migration such as the influence of the surrounding microenvironment [7–9] or the flow of actin within a migrating cell [10,11], the connection between individual cell properties and collective behaviour remains unclear.

To infer single-cell phenotypes from collective migration behaviour requires additional information beyond that provided by metrics such as time to wound closure. Particle image velocimetry (PIV) allows us to extract not only boundary motion from time-lapse imaging data but also the entire flow field of cell motion, which includes features at the scale of single cells or smaller. Since their introduction into cell migration research several years ago, PIV flow fields have rapidly emerged as a powerful tool and have been used to analyse a wide variety of collective cell behaviours including correlated motion [12,13], vortices [14], patterns of stresses within the cell sheet [15] and changes to collective migration during malignancy [16]. Notable prior work on large-scale flow fields generated by coupled polar entities was carried out in the context of soft condensed matter, starting with liquid crystals and most recently active matter [17,18]. Our focus

is on the heterogeneity and time variability that is a hallmark of living systems, including most notably sources of heterogeneity such as cellular activity and leader cells that are thought to control collective behaviour in living systems.

Here, we link detailed metrics of collective behaviour derived from PIV data with simulations of collective cell motion that explicitly model the behaviour of individual cells. By linking experiments and simulations, we can infer likely single-cell behaviour from collective motion phenotypes. Collective cell migration has been studied using a wide variety of modelling techniques [13,19–25]. These modelling techniques have been used to explore a variety of factors involved in collective migration that are difficult to access experimentally, including the effect of matrix geometry on migration strategies [26] and the maturation of cell contacts within a monolayer [27]. Several studies have noted the important link between cell motility and polarity [27–29], a feature of migration that we explore further.

Our work links previously published experimental observations on collective migration of MCF10A breast epithelial cells [30] and a previously published model of collective migration [20,31–33] to elucidate which properties of individual cells are most consistent with the observed multi-cell collective migration behaviour. The experimental data show changes in collective behaviour on large length scales that span the cell monolayer. In the cases of collective behaviour, cell motion contributes to the radial expansion of the monolayer across millimetre scales, while in other, less collective cases, only those cells near the outer edge contribute to monolayer expansion. We show that these changes in large-scale migration patterns can be recreated in our model without requiring large-scale gradients or 'leader cells' (a subpopulation of cells at the edge of the monolayer that has different properties from cells within the bulk of the monolayer). Our modelling results suggest that the experimentally observed changes in collective behaviour are consistent with simply decreasing the activity of individual cells as long as the cells have a strong coupling between their velocity and preferred motility direction.

2. Material and methods

2.1. MCF10A dataset

We analyse a previously published set of time-lapse images of MCF10A (breast epithelial cells) migrating in collective sheets [30,34]. These cells, which were plated in a circular monolayer, migrate on a collagen IV coated glass surface and phase contrast images were taken every 3 min for a total of 1000 min (16.6 h). The dataset includes cells migrating in normal cell culture media (referred to as 1 : 1) and cells migrating in a dilution of this culture media (referred to as 1 : 5). This change decreases the horse serum, insulin, EGF, hydrocortisone and cholera toxin concentrations to 20% of their full media values (e.g. horse serum at a concentration of 1% instead of 5%).

2.2. Migration analysis

Phase contrast images were analysed with PIV using the MatPIV toolbox (J. Kristian Sveen, GNU general public licence) for Matlab (MathWorks, Inc.). Multiple iterations of interrogation window sizes were used: two iterations of 64 × 64 pixel windows were followed by two iterations using 32 × 32 pixel windows. A 50% overlap was used for each interrogation step. Several steps were taken to increase the quality of our PIV flow fields. The size of our interrogation windows was chosen to provide of the order of 10 features per window, suggested as a good rule of thumb for a clear PIV signal [35]. We also run a multi-pass algorithm that first uses a larger window size to reduce noise. The resulting flow field uses information about the relative height of the chosen cross-correlation peak and all possible correlation peaks as a signal-to-noise ratio to further filter the PIV flow field; outliers were detected using a signal-to-noise threshold of 1.3.

Custom Matlab segmentation code was used to find the leading front of the cell monolayer. The phase contrast images were Sobel filtered followed by median filtering and morphological opening to clean the binary image before finding the perimeter of the objects in the image. The edge coordinates were then found using a Matlab implementation of Dijkstra's algorithm ('dijsktra path finder' by Sebastien PARIS, available on the Matlab File Exchange at mathworks.com). In combination with the microscope stage positions, this edge was used to fit the cell monolayer to a circle (see electronic supplementary material, figure S1). The effective radius of the monolayer and the centre position were used to define regions of the cell monolayer for later migration analysis. Speed and radial velocity values were averaged over theta to create radial profiles of motion.

Velocity correlations were calculated as

$$C(\Delta r) = \frac{\sum_{r,t} (\boldsymbol{v}(r) - \bar{v}) \cdot (\boldsymbol{v}(r+\Delta r) - \bar{v})}{\sigma_v^2}.$$

In this case, $v(r)$ is the velocity at a location r within the cell sheet. The correlation values are averaged over all r within the region $0.5 < r/R < 0.75$ and over all times. In this equation and throughout, r refers to the location within the cell monolayer with respect to the monolayer centre and R refers to the size of the monolayer. These correlation values were fitted to a double exponential of the form

$$C(\Delta r) = A\mathrm{e}^{-r/L_{c1}} + B\mathrm{e}^{-r/L_{c2}} + (1 - A - B).$$

2.3. Simulations

Our model is based on earlier work [20,32] and includes cell growth and division, motility forces, friction forces, and volume exclusion and adhesion between neighbouring cells, as shown in figure 2*a*. In the model, two point particles represent a single cell with a size given by the inter-particle distance r. The equation of motion for each particle is given by

$$\frac{\mathrm{d}\boldsymbol{p}}{\mathrm{d}t} = \boldsymbol{m} + \boldsymbol{F}_{\mathrm{exp}} + \boldsymbol{F}_{\mathrm{int}} + \boldsymbol{F}_{\mathrm{B}} + \sum_{r \le R_{\mathrm{CC}}} (\boldsymbol{F}_{\mathrm{rep/ad}} + \boldsymbol{F}_{\mathrm{df}}).$$

Here, $\boldsymbol{m}$ is the motility force (discussed further below) and its value, along with all other parameter values, is given in electronic supplementary material, table S1. Cell growth is simulated through a repulsion force $\boldsymbol{F}_{\mathrm{exp}} = -B/(r+1)^2\hat{r}$, where B is an expansion factor and $\hat{r}$ is the unit vector parallel to the line connecting the two particles. Cell division is incorporated as follows: after the cell size reaches a threshold R_{div}, it divides at a constant rate k_{div}, after which two new particles are placed a distance r_{div} away from the particles constituting the old cell. $\boldsymbol{F}_{\mathrm{int}}$ represents the intracellular friction force between particles constituting the same cell and is determined by the coefficient ξ_{int}. Cell–substrate friction is assumed to be proportional to the cell velocity, resulting in $\boldsymbol{F}_{\mathrm{B}} = -\xi_{\mathrm{B}}\boldsymbol{v}$. The last two forces in the equation of motion act only within a distance of $r \le R_{\mathrm{CC}}$ and represent volume exclusion and adhesion of cells ($\boldsymbol{F}_{\mathrm{rep/ad}}$) and friction forces that oppose the relative motion of cells with a friction coefficient ξ_{df} ($\boldsymbol{F}_{\mathrm{df}}$). Details of the latter can be found in Basan *et al.* [32], while the former has two terms: a short-range repulsive term, which prevents cell–cell overlap and is parametrized by f_0, and a long-range adhesive force with a strength determined by f_1. The

equation for volume exclusion and adhesion is of the form

$$\boldsymbol{F}_{\mathrm{rep/ad}} = -\left(\mathrm{f}_0\left(\frac{1}{r-1}\right) - f_1\right)\hat{r}.$$

The orientation of the motility force $\boldsymbol{m}$ is such that it tends to align with the cell's velocity $\boldsymbol{v}$. Specifically, this motility–velocity alignment coupling is implemented by assuming two states of the cell: a motile state and a non-motile state. Cells in the non-motile state exert no motility force while cells in the motile state generate a motility force with a fixed magnitude in a random direction. The transition from the non-motile state to the motile state is determined by a constant rate k_{wake} by generating a motility force with a fixed magnitude in a random direction. The transition rate from the motile state back to the non-motile state depends on the motility–velocity alignment, quantified by $\boldsymbol{m}\cdot\boldsymbol{v}$. In Basan *et al.* [20], this transition rate could take on only two values: low for aligned cells ($\boldsymbol{m}\cdot\boldsymbol{v} > 0$) or high for non-aligned cells ($\boldsymbol{m}\cdot\boldsymbol{v} < 0$). This bias results in a higher ratio of aligned cells versus non-aligned cells in the motile state and provides an alignment mechanism. In this study, we use a continuous form of the transition rate to the non-motile state that depends on the degree of alignment

$$k'_{\mathrm{sleep}} = \frac{(k_0 - k_1)(1 + \tanh(-(\boldsymbol{m}\cdot\boldsymbol{v})/k_{\mathrm{mv}}))}{2} + k_1.$$

Thus, this rate ranges from k_1 for aligned cells to k_0 for non-aligned cells while the transition between these two rates is determined by k_{mv}; when $k_{\mathrm{mv}} \ll |\boldsymbol{m}||\boldsymbol{v}|$ the transition rate approaches the aligned and not-aligned binary case of Basan *et al.* [20].

Our transition rate was further modified to account for the effect of leader cells, i.e. cells near the edge of the colony that preferentially move outward. To this end, we multiplied the above transition rate with a spatially dependent prefactor so that the final form for particle i is $k_{\mathrm{sleep}} = \exp(k_{\mathrm{Rm}}\boldsymbol{m}_i\cdot\boldsymbol{R}_i)\, k'_{\mathrm{sleep}}$. Here $\boldsymbol{R}_i$ is a spatial average of the particle's neighbours: $\boldsymbol{R}_i = \sum_{\mathrm{neighbors}} \boldsymbol{r}_{ij}$, where $\boldsymbol{r}_{ij} = \boldsymbol{r}_j - \boldsymbol{r}_i$ is the relative position of cells i and j. The parameter k_{Rm} determines the strength of the leader cell effect. Neighbour cells are defined as cells within the range of non-zero cell interactions, i.e. $r \le R_{\mathrm{CC}}$. Cells far from the edge are surrounded by other cells such that $\boldsymbol{R} \approx 0$ and the prefactor is close to one. Cells near the edge, however, have only neighbours inside the colony, resulting in a value of $\boldsymbol{R}$ that points inward. Consequently, k_{sleep} is smaller for cells near the edge that have their motility vector pointing outwards, leading to 'leader' cells that move outward. In the standard set of parameters (see electronic supplementary material, table S1), $k_{\mathrm{Rm}} = 0$ and there is no leader cell effect.

The simulation starts with 200 spheres (and thus 100 cells) randomly located within a square box of 10×10, measured in units of l_0 (see electronic supplementary material, figure S2). The initial velocity for all the spheres is taken to be zero. The first 10 frames of the simulated data (100 t_0) were discarded before migration analysis to remove artefacts from low cell number monolayers. Particle positions and velocities were interpolated to a grid to compare with experimental PIV results. The edge of the simulated monolayer was found based on the particle positions and fitted to a circle. As with the experimental results, this edge was used to define radial regions of the monolayer and to create profiles of speed and radial velocity. Migration analysis was then carried out in the same manner as previously described for the experimental data.

We should note that the length scale of the model, l_0, can be related to experimental values by comparing it to the experimental division size. In our simulations, we choose the threshold distance for cell division to be $0.4l_0$. This should be of the same order of magnitude as the average cell size, which is approximately 40 µm, resulting in $l_0 \approx 100$ µm. The simulation time can then be determined by comparing the mean speed of cells in the simulation ($\approx 0.025 l_0/t_0 = 2.5\ \mu\mathrm{m}/t_0$) to the mean speed in the experiment ($\approx 0.25\ \mu\mathrm{m\ min}^{-1}$) which leads to $t_0 \approx 10$ min. We can then verify that the relative growth rate in the simulation is consistent with the relative growth rate observed in the experiments, as shown in electronic supplementary material, figure S4. This comparison suggests that the experiments and simulations are on the same scale for growth, but note that we do not attempt to fit the multiple model parameters to the data.

3. Results

To study large spatial scale migration patterns in epithelial MCF10A cells, we analyse a previously published set of time-lapse images of a circular cell monolayer [30]. The cells were imaged near the edge (figure 1*a* and electronic supplementary material, movie S1) and in the centre of the monolayer; a schematic of the imaging fields of view is shown in figure 1*b*. The multiple fields of view allow us to investigate migration behaviour as a function of location within the monolayer; figure 1*c* shows an example kymograph of speed within a monolayer. There are heterogeneities in speed over both the 16 h time course and approximately 4 mm spatial scale of the cell sheet, yet there is a trend towards higher speed at the edge of the monolayer. This trend can be seen in the time-averaged speed curves in figure 1*d*.

Although the cell speed increases near the edge in all experiments, there are changes in the overall speed depending on the media dilution (1 : 1 versus 1 : 5) and day-to-day variability in the experiments (see electronic supplementary material, figure S3, for a discussion of this variability). In addition to measuring speed, which indicates how active the cells are, we also determine the radial velocity as a measure of how well the cells' motion contributes to the overall expansion of the cell sheet. As shown in figure 1*e*, when the overall motion is slow, we see a decreased radial velocity, as would be expected.

In addition to this quantitative change, however, we also see a qualitative change in which some experiments exhibit a concave curve (black squares in figure 1*e*) while others—those with lower cell speeds—show a convex curve (red circles in figure 1*e*). Since radial velocity is the component of cell motion that contributes to the collective expansion of the monolayer, this suggests changes in the collective behaviour of the cell sheet. In those cases with lower overall cell speed, the cells near the centre of the monolayer move in all directions; since radial velocity can be positive or negative, these values average out to near zero in the centre region. In the cases with higher overall speed, however, cells throughout large regions of the cell monolayer contribute to the overall expansion. Thus, we use the shape of the radial velocity curve as one indicator of how cooperatively the cells move—when the curve is concave, cooperative motion spreads through the cell monolayer, but when the curve is convex the cells move less collectively.

To explore how individual cell properties affect the qualitative large-scale changes seen in this dataset, we compare the experimental results to simulations using a previously published model [20,31,32]. In this model, each cell is represented by two particles that move according to the forces acting upon them (shown schematically in figure 2*a*). These forces, further detailed in the Material and methods section, include friction forces, motility forces, cell–cell interaction forces and a force representing cell growth. Cell division is initiated once the

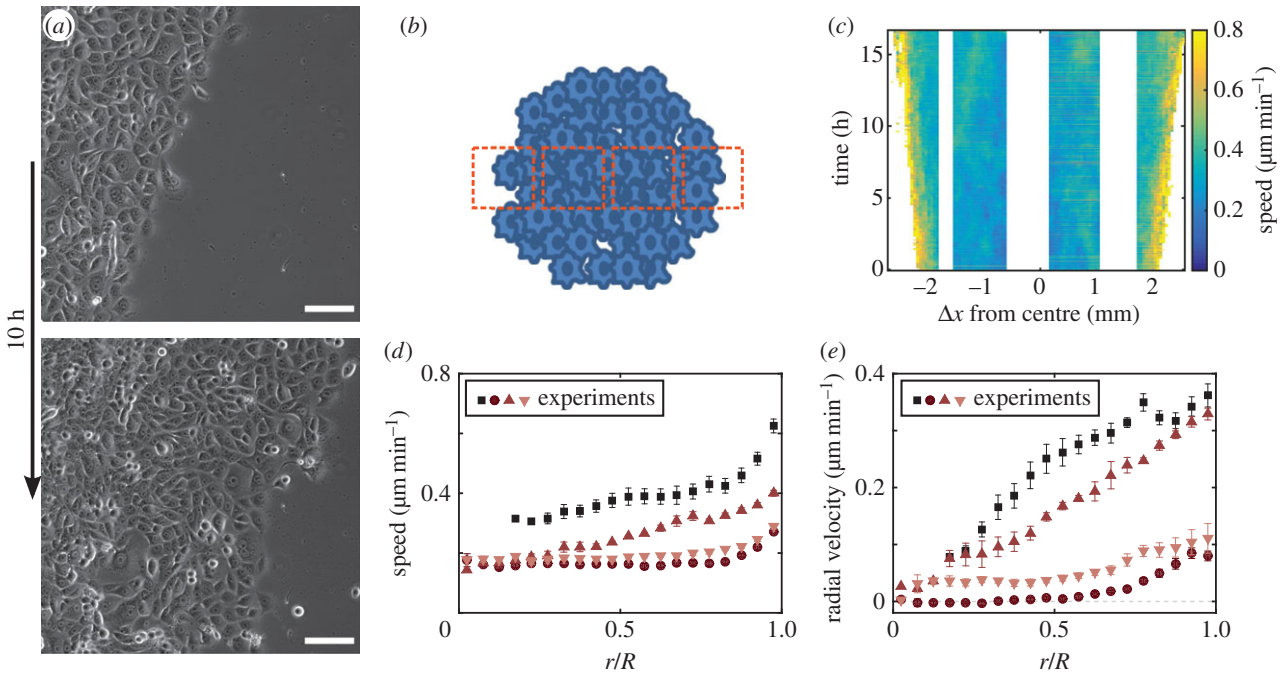

Figure 1. MCF10A cell sheets migrate collectively over 10 h (*a*; scale bar 100 μm). The cells are plated in a circular monolayer and multiple fields of view scanning the diameter are imaged (*b*; see also electronic supplementary material, figure S1). Over time, these regions show different speed profiles with larger speeds seen near the edge of the cell sheet (*c*). The experiments show variability in overall speed, but cells near the edge remain faster (*d*). In low speed cases, the radial velocity decreases and also qualitatively changes pattern (*e*). Error bars in (*d*,*e*) represent the standard error of the mean of four technical replicates performed on the same day in full media (1 : 1, black squares) or diluted media (1 : 5, red circles and triangles).

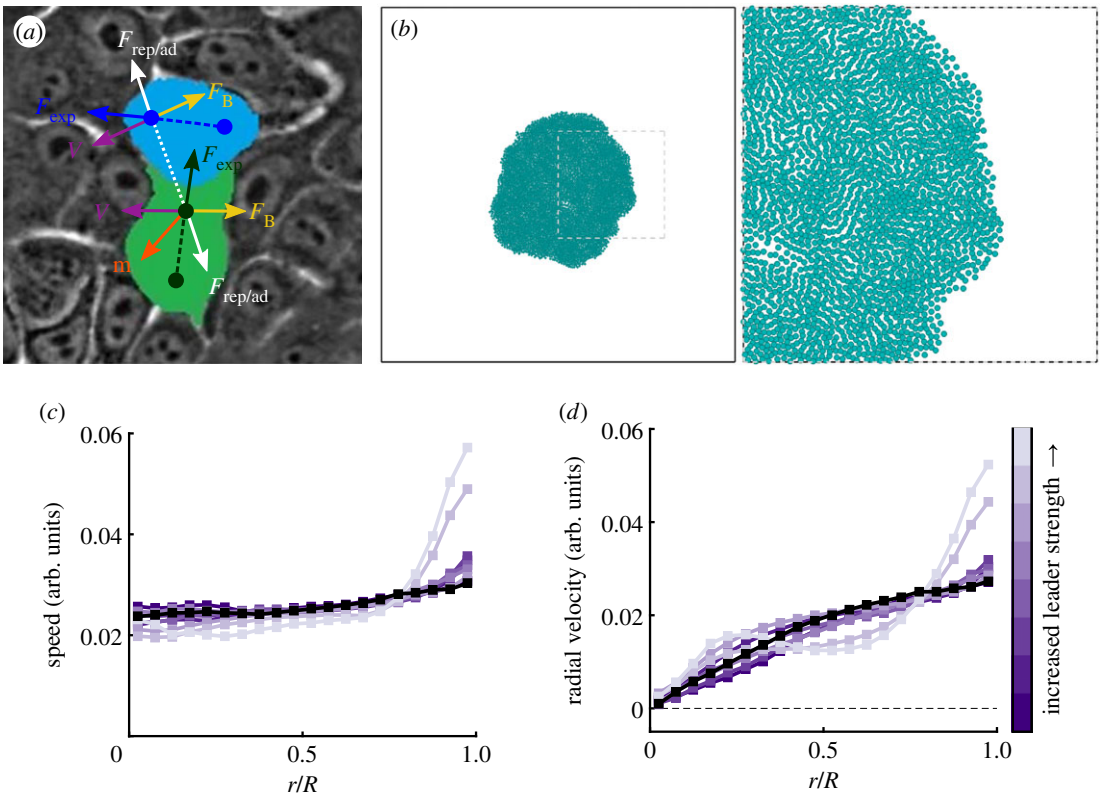

Figure 2. Multiple forces act on the simulated cells (*a*). Each cell is composed of two particles, which feel a cell expansion force (F_{exp}). The particles also have a velocity (V) and experience friction between the cell and substrate (F_B). Cells interact through a force that is repulsive at short distances and attractive at intermediate distances ($F_{rep/ad}$). Cells may be in a sleep state (*a*, blue cell) or awake state (*a*, green cell); only awake cells experience a motility force (m) that provides a preferred direction of motion. Particles also experience friction and noise forces that are not shown. Electronic supplementary material, movie S2, shows simulated cell motion using the standard parameter set; a still image is shown in (*b*). Simulated cells show a similar speed profile to the experimental results; the addition of leader cells increases the speed at the edge of the monolayer (*c*). Simulated leader cells increase radial velocity, but do not cause the qualitative change in radial velocity seen experimentally (*d*). From dark purple to light purple, k_{Rm}—which controls the leader cell strength—is set to 0.01, 0.05, 0.1, 0.25, 0.5, 1, 5 and 10, while the black curve represents the standard simulation set with no leader cells, $k_{Rm} = 0$ (*c*,*d*).

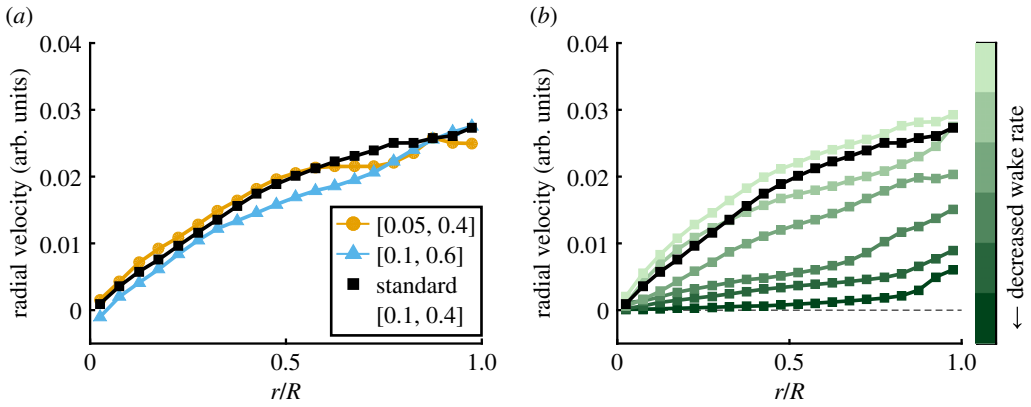

Figure 3. Decreasing proliferation rate does not qualitatively change the radial velocity (*a*); legend pairs indicate [k_{div}, R_{div}] parameter values. Decreasing the rate at which non-motile cells 'wake' causes a transition from a concave to a convex curve (*b*). Wake rate parameter values (k_{wake}) in (*b*) are 0.03, 0.05, 0.1, 0.2, 0.3 and 0.5 from dark green to light green with the standard wake rate of 0.4 shown in black. Speed profiles for these simulations are shown in electronic supplementary material, figure S6.

distance between the particles exceeds a threshold. Cells can be either motile or non-motile, and the transition rate between these two states is chosen such that motile cells tend to align their motility force (the force that pushes a cell in a preferred direction) with their velocity. Alignment between the cell's motility force and velocity has previously been shown to lead to 'go with the flow' dynamics [20]; alignment between velocity and a preferred direction is also a feature of active matter models of cell migration [36].

Simulated monolayers in this model using the standard parameters (see electronic supplementary material, table S1) and in the absence of leader cells show a radial expansion similar to the MCF10A experimental system, and have increased speed near the edge of the monolayer (see figure 2*b*, black curve, and electronic supplementary material, movie S2). Simulations with the standard parameter set also show an increased radial velocity near the leading edge of the cell sheet and a concave radial velocity profile in the centre of the cell monolayer (figure 2*c*, black curve), similar to the experimental results with faster cells (figure 1*c*, black squares).

In a first computational test, we explore whether introducing an active subpopulation of cells near the edge, leader cells, may be sufficient to cause the experimentally observed change in velocity profile shown in figure 1. Leader cells near the leading edge of migrating cell groups are seen in many collective migration systems [37] and have often been observed at the tip of finger-like protrusions of epithelial sheets [38,39]. Many studies have also found that multicellular rows of leader cells can emerge in epithelial wound healing [37,40]. The exposure to extracellular matrix on one side of the cells and cell–cell adhesion on the other, as found at the leading edge of cell sheets, can cause cells to change their morphology or upregulate distinct signalling pathways [37–40].

In our simulation, leader cells are included by making the transition rate between the motile and non-motile state of motion dependent on the spatial location of the cell (see Material and methods). As seen in figure 2*c*, increasing the strength of this leader cell effect can lead to increased speeds near the monolayer edge. However, this increase is not accompanied by a qualitative change from concave to convex radial velocity profiles (figure 2*d*), suggesting that another mechanism is responsible for the experimentally observed change in the radial velocity profiles. At high leader cell strengths, the profile does qualitatively change in that it shows a flat profile, in part, of the sheet, but this is due to an instability of the boundary shape. This instability results in the formation of fingering structures at the leading edge (see electronic supplementary material, movie S3), similar to the behaviour seen in a previous study which found leading tip cells in finger-like protrusions of epithelial sheets [39].

We next hypothesized that the proliferation rate may affect the phenotype. Changing proliferation rates in our simulations, however, does not change the simulated speed profile (electronic supplementary material, figure S3*a*) or the radial velocity profile (figure 3*a*). We should note that for low proliferation rates (less than 10% of the standard parameter value for division), the monolayer begins to break apart (see electronic supplementary material, figure S7). In this case, the cell sheet can no longer be fitted to a circle for radial analysis. The disassociation of the monolayer at low proliferation rates agrees with a hypothesis that cell proliferation is used to fill in the gaps left by a migrating monolayer rather than as a mechanism for pushing migration forward [39,41].

In a third set of computational trials, we determined how changes in the 'wake rate' parameter affect velocity profiles. The wake rate parameter controls how often cells switch from a state without a preferred direction of motion to a 'motile' state in which the cells experience an additional force that indicates a preferred direction of motion and thus controls how 'active' the cells are within the monolayer. The motility force plays the role of a biomechanical polarity within the cell, but does not distinguish which of the many mechanical and chemical stimuli that lead to polarity changes [42] are experienced by the cell. It may be expected that the cases of reduced speed in the experimental data correspond to decreased activity in the cells.

Our simulations reveal that decreasing the wake rate leads to an overall lower speed (electronic supplementary material, figure S3*b* and movie S4) and, as shown in figure 3*b*, a qualitatively different radial velocity profile. Specifically, decreasing the wake rate leads to a transition from behaviour where cells across the radius of the monolayer move outward, showing radially expanding motion, to a state where only those cells near the edge move cooperatively outward. As a result, the radial velocity profile changes from a concave one to a convex one consistent with the experimentally observed changes in radial velocity and collective behaviour.

We next determined how the coupling between the cell's velocity and motility force, parametrized by k_{mv}, affects the

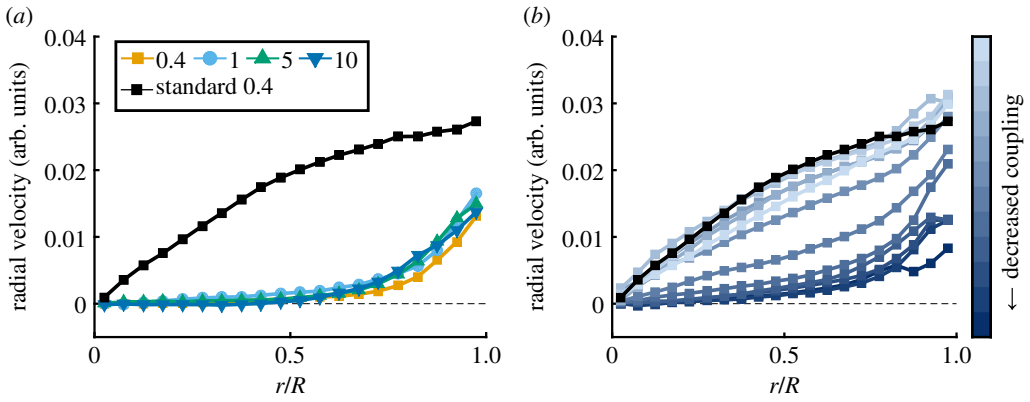

Figure 4. If velocity–motility coupling is removed (*a*), changing the wake rate cannot capture the experimentally seen results (k_{wake} value shown in legend; standard parameter set with coupling and $k_{wake} = 0.4$ shown in black). Radial velocity undergoes a qualitative change as the coupling is increased which is similar to the change seen in the MCF10A experiments (*b*); from dark blue to light blue the coupling parameter k_{mv} is set to 0.1, 0.05, 0.04, 0.035, 0.03, 0.025, 0.02, 0.015, 0.01, 0.005, 0.001 and 0.0001. The standard k_{mv} value of 0.00001 is shown in black. Smaller values of k_{mv} indicate a stronger coupling strength. Speed profiles for these simulations are shown in electronic supplementary material, figure S8.

velocity profiles. This alignment coupling leads to higher sleep rates for those cells that have velocity and motility forces pointing in opposing directions. Interestingly, if the coupling between the motility force and velocity is removed, the simulations always show convex radial velocity profiles (i.e. decreased collective migration), even for large values of the wake rate (figure 4*a* and electronic supplementary material, movie S5). This suggests the strength of this coupling may also play a role in migration. Indeed, using otherwise standard parameters but decreasing the strength of the coupling between velocity and motility can cause a transition from a concave to a convex radial velocity curve (figure 4*b*; electronic supplementary material, movie S6). Thus, causing each cell to have strong alignment between its motility direction and its current velocity leads to more active behaviour (concave velocity profiles), while motility that is not strongly coupled leads to convex velocity profiles similar to those seen in the less active experiments.

To probe further the changes in collective behaviour that may accompany the observed changes in radial velocity, we calculate velocity correlations in the region between the centre and the edge of the monolayer ($0.5 < r/R < 0.75$). This range was chosen to correspond to the region where we see experimental changes in the radial velocity profile. The spatial autocorrelation of velocity does not distinguish between types of behaviour such as divergence or rotation, but rather provides a metric for similarity of motion across the cell sheet; this similarity would be expected when cells migrate cooperatively. As shown in figure 5*a*, experimental conditions with decreased speed and convex radial velocity correspond to the cases of less correlated motion within the cell sheet. To determine whether this result is consistent with our computational model we compute the spatial correlation in our simulated trials. We focus on the perturbations—reducing the wake rate and decreasing the motility–velocity coupling—that are able to reproduce the qualitative change in radial velocity profiles. We find that both decreasing the wake rate (figure 5*b*) and decreasing the coupling (figure 5*c*) result in a reduction of the spatial correlation consistent with the experimental results.

We compare the observed changes in radial velocity and correlated motion within the cell sheet by calculating characteristic length scales from the velocity autocorrelation. Both the experimental PIV flow fields and the simulated cell motion naturally include two length scales: the experimental data include both subcellular and multicellular flows and the simulated data include the motion of both particles that make up a cell. To address this, we fit the correlation curves to a double exponential and indeed find that the smaller of the two experimental length scales (approx. 15 µm) is of the order of the cell size (figure 5*d*). We also find that the larger length scale, which indicates multicellular cooperation, shows an increasing trend with increasing radial velocity for both the experimental data and model results (figure 5*d–f*), further suggesting that the observed change in radial velocity corresponds to a change in multicellular cooperation.

4. Discussion

Here we provide insight into the single-cell behaviour underlying collective migration by comparing experimental data to a model of collective migration. The emergent behaviour of collective cell sheets that results from changing the properties of individual cells is difficult to predict and to probe experimentally. To investigate the connection between individual and collective behaviour, we use PIV-based migration data to measure motion that spans a wide variety of scales; the length scales studied vary from that of a single cell to a monolayer composed of thousands of cells. By comparing simulation and experiment across these scales, we provide insight into collective behaviour changes observed in epithelial MCF10A cells. Cells moving at higher speeds show a larger region of radial expansive motion than slowly moving cells (figure 1), suggesting changes in their collective behaviour.

Leader cells have been found in a variety of experimental systems and in previous studies have been found to recruit following cells to move directionally outward through a Viscek-like coupling [43]. We show here that they are not necessary, however, to recapture large-scale changes in collective migration in our model of epithelial sheet migration (figure 2). We also show that changes in proliferation are unlikely to be the cause of the observed large-scale changes (figure 3*a*). Experimental changes in activity can be compared with the wake rate in the simulations; this parameter is related to the simulated cells' ability to switch between a non-motile and motile state. Here we find that changes in the wake rate

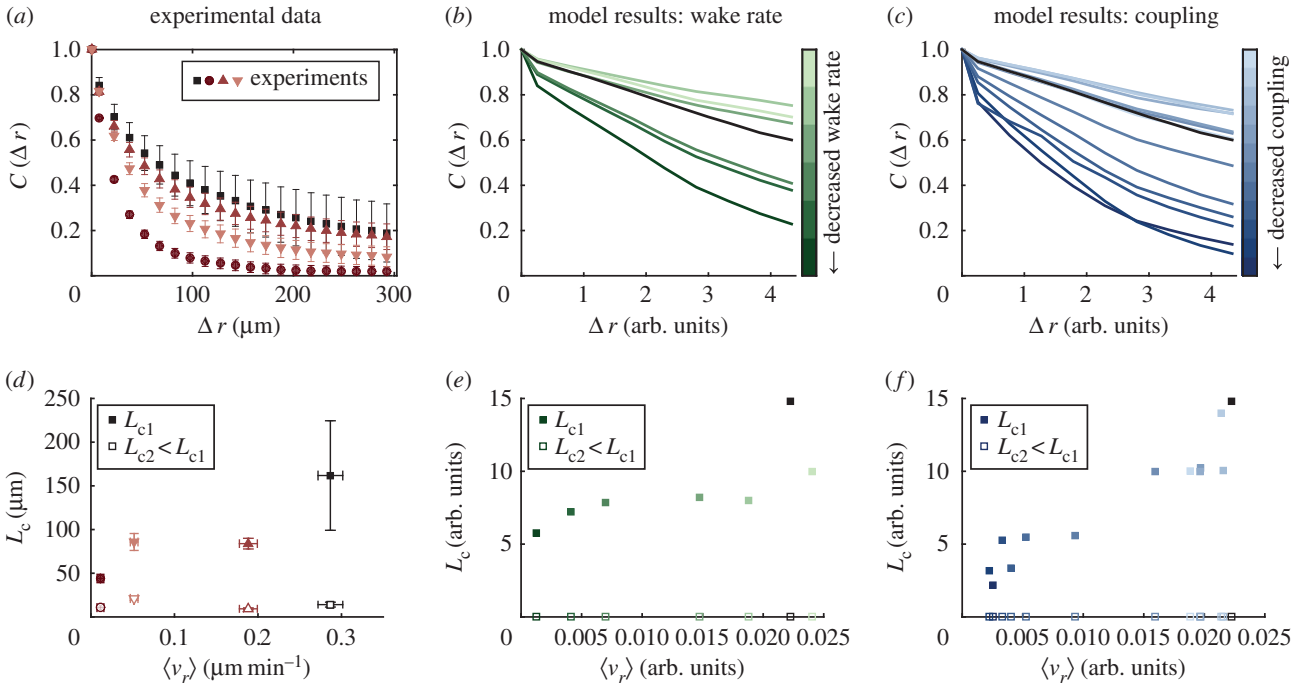

Figure 5. In the case of decreased experimental speed (*a*,*d*), decreased wake rate (*b*,*e*) and decreased coupling (*c*,*f*), the cells are less correlated in their motion. (*a*–*c*) Time-averaged velocity correlations (see Material and methods) in the transition region, defined as $0.5 < r/R < 0.75$. (*d*–*f*) The characteristic length scales (L_c) determined from a double exponential fit to the curves in (*a*–*c*). Error bars on the experimental data represent the standard error of the mean of four technical replicates. Wake rate parameter values (k_{wake}) in (*b*,*e*) are 0.03, 0.05, 0.1, 0.2, 0.3 and 0.5 from dark green to light green. From dark blue to light blue in (*c*,*f*), the coupling parameter k_{mv} is set to 0.1, 0.05, 0.04, 0.035, 0.03, 0.025, 0.02, 0.015, 0.01, 0.005, 0.001 and 0.0001. Smaller values indicate a stronger coupling strength. The standard parameter set ($k_{wake} = 0.4$ and $k_{mv} = 0.00001$) is shown in black in (*b*,*c*,*e*,*f*).

can lead to the experimentally observed changes in collective behaviour (figure 3*b*).

Interestingly, changing the wake rate has no effect without implementing alignment coupling between the cells' motility and velocity (figure 4*a*). Previous work on this collective migration model has shown that this coupling leads to a 'go with the flow' dynamic [20]; the coupling is implemented such that cells with misaligned motility and velocity vectors are more likely to transition to a non-motile state. The motility force gives the cells a preferred direction of motion, and in that sense, it can be viewed as a biomechanical cell polarity. The ability to align this biomechanical polarity with the direction of motion of a cell indicates that a cell is able to sense resistance to motion and adapt its biomechanical machinery to push in a direction in which the cell is actually able to move. Thus, the strength of this coupling indicates how sensitive a cell is to its mechanical environment, and it is not surprising that changing this motility to velocity coupling changes the collective behaviour of the cells (figure 4*b*). This result agrees with previous work which suggests that propagating waves of cell stretching, which leave cells with more elongated and polarized shapes, are followed by waves of increased directionality in sheets of epithelial cells [44].

Ultimately, the motility coupling strength provides a simple sensor of the surrounding tissue and leads to cells that are best able to follow a path of least resistance, since increased motion along the path of least resistance will lead to feedback with alignment of the motility force. Changing this coupling strength can cause large-scale changes in cell migration without explicitly changing the interactions between neighbouring cells or invoking leader cells. Increasing activity within the cell sheet has a similar effect as it gives the cells more opportunities to be motile at the same time and thus follow other cells on paths of least resistance. When combined with a strong sense of polarity, this activity can then lead to increasing cooperativity over time as the cells have more opportunities to align their motion.

We thus find in our simulations that the emergent behaviour of a simple model system can explain large-scale changes in collective behaviour without the need to specify large-scale features explicitly. We identify cell activity and the coupling between biomechanical polarity and motion as two interesting features of individual cell behaviour that can lead to large-scale collective behaviours. Our study demonstrated that PIV measurements may be used in conjunction with simulations to infer detailed biomechanical single-cell phenotypes from the types of collective migration assays that are commonly used in drug discovery and cancer research.

Data accessibility. Supporting data for this paper are stored in the Digital Repository at the University of Maryland: DRUM (doi:10.13016/M2855R) [34].

Authors' contributions. R.M.L. performed image analysis on the MCF10A dataset, participated in data analysis and drafted the manuscript; H.Y. carried out the simulations and participated in data analysis; W.-J.R. and W.L. conceived of the study and coordinated the study. All authors edited the manuscript and gave their final approval for publication.

Competing interests. The authors have no competing interests.

Funding. This work was carried out with financial support to R.M.L. and W.L. from a NSF-Physics of Living Systems grant (PHY1205965). R.M.L. was additionally supported by the JCM Foundation through an ARCS/MWC Scholar Award. W.-J.R. and H.Y. were supported by NIH grant no. P01 GM078586 and NSF grant no. DMS 1309542.

Acknowledgements. We thank the members of the Losert lab and Carole Parent's lab (LCMB, CCR, NCI, National Institutes of Health) for their discussion and suggestions. We also thank the anonymous reviewers for their useful suggestions.

References

1. Weijer CJ. 2009 Collective cell migration in development. *J. Cell Sci.* **122**, 3215–3223. (doi:10.1242/jcs.036517)
2. Theveneau E, Mayor R. 2012 Neural crest delamination and migration: from epithelium-to-mesenchyme transition to collective cell migration. *Dev. Biol.* **366**, 34–54. (doi:10.1016/j.ydbio.2011.12.041)
3. Martin P. 1997 Wound healing—aiming for perfect skin regeneration. *Science* **276**, 75–81. (doi:10.1126/science.276.5309.75)
4. Anon E, Serra-Picamal X, Hersen P, Gauthier NC, Sheetz MP, Trepat X, Ladoux B. 2012 Cell crawling mediates collective cell migration to close undamaged epithelial gaps. *Proc. Natl Acad. Sci. USA* **109**, 10 891–10 896. (doi:10.1073/pnas.1117814109)
5. Friedl P, Gilmour D. 2009 Collective cell migration in morphogenesis, regeneration and cancer. *Nat. Rev. Mol. Cell Biol.* **10**, 445–457. (doi:10.1038/nrm2720)
6. Cheung KJ, Gabrielson E, Werb Z, Ewald AJ. 2013 Collective invasion in breast cancer requires a conserved basal epithelial program. *Cell* **155**, 1639–1651. (doi:10.1016/j.cell.2013.11.029)
7. Doyle AD, Wang FW, Matsumoto K, Yamada KM. 2009 One-dimensional topography underlies three-dimensional fibrillar cell migration. *J. Cell Biol.* **184**, 481–490. (doi:10.1083/jcb.200810041)
8. Ventre M, Natale CF, Rianna C, Netti PA. 2014 Topographic cell instructive patterns to control cell adhesion, polarization and migration. *J. R. Soc. Interface* **11**, 20140687. (doi:10.1098/rsif.2014.0687)
9. Charras GT, Sahai E. 2014 Physical influences of the extracellular environment on cell migration. *Nat. Rev. Mol. Cell Biol.* **15**, 813–824. (doi:10.1038/nrm3897)
10. Allard J, Mogilner A. 2013 Traveling waves in actin dynamics and cell motility. *Curr. Opin. Cell Biol.* **25**, 107–115. (doi:10.1016/j.ceb.2012.08.012)
11. Maiuri P *et al.* 2015 Actin flows mediate a universal coupling between cell speed and cell persistence. *Cell* **161**, 374–386. (doi:10.1016/j.cell.2015.01.056)
12. Petitjean L, Reffay M, Grasland-Mongrain E, Poujade M, Ladoux B, Buguin A, Silberzan P. 2010 Velocity fields in a collectively migrating epithelium. *Biophys. J.* **98**, 1790–1800. (doi:10.1016/j.bpj.2010.01.030)
13. Sepúlveda N, Petitjean L, Cochet O, Grasland-Mongrain E, Silberzan P, Hakim V. 2013 Collective cell motion in an epithelial sheet can be quantitatively described by a stochastic interacting particle model. *PLoS Comput. Biol.* **9**, e1002944. (doi:10.1371/journal.pcbi.1002944)
14. Angelini TE, Hannezo E, Trepat X, Fredberg JJ, Weitz DA. 2010 Cell migration driven by cooperative substrate deformation patterns. *Phys. Rev. Lett.* **104**, 168104. (doi:10.1103/PhysRevLett.104.168104)
15. Serra-Picamal X *et al.* 2012 Mechanical waves during tissue expansion. *Nat. Phys.* **8**, 628–634. (doi:10.1038/nphys2355)
16. Weiger MC, Vedham V, Stuelten CH, Shou K, Herrera M, Sato M, Losert W, Parent CA, Ahmad A. 2013 Real-time motion analysis reveals cell directionality as an indicator of breast cancer progression. *PLoS ONE* **8**, e58859. (doi:10.1371/journal.pone.0058859)
17. Marchetti MC, Joanny JF, Ramaswamy S, Liverpool TB, Prost J. 2013 Hydrodynamics of soft active matter. *Rev. Mod. Phys.* **85**, 1143–1189. (doi:10.1103/RevModPhys.85.1143)
18. Hagan MF, Baskaran A. 2016 Emergent self-organization in active materials. *Curr. Opin. Cell Biol.* **38**, 74–80. (doi:10.1016/j.ceb.2016.02.020)
19. Vicsek T, Zafiris A. 2012 Collective motion. *Phys Rep.* **517**, 71–410. (doi:10.1016/j.physrep.2012.03.004)
20. Basan M, Elgeti J, Hannezo E, Rappel W-J, Levine H. 2013 Alignment of cellular motility forces with tissue flow as a mechanism for efficient wound healing. *Proc. Natl Acad. Sci. USA* **110**, 2452–2459. (doi:10.1073/pnas.1219937110)
21. Löber J, Ziebert F, Aranson IS. 2015 Collisions of deformable cells lead to collective migration. *Sci. Rep.* **5**, 9172. (doi:10.1038/srep09172)
22. Graner F, Glazier JA. 1992 Simulation of biological cell sorting using a two-dimensional extended Potts model. *Phys. Rev. Lett.* **69**, 2013–2016. (doi:10.1103/PhysRevLett.69.2013)
23. Camley BA, Rappel W-J. 2017 Physical models of collective cell motility: from cell to tissue. *J. Phys. D* **50**, 113002. (doi:10.1088/1361-6463/aa56fe)
24. Vedula SRK, Leong MC, Lai TL, Hersen P, Kabla AJ, Lim CT, Ladoux B. 2012 Emerging modes of collective cell migration induced by geometrical constraints. *Proc. Natl Acad. Sci. USA* **109**, 12 974–12 979. (doi:10.1073/pnas.1119313109)
25. Gov NS. 2014 Collective cell migration. In *Cell and matrix mechanics* (eds R Kaunas, A Zemel), pp. 219–238. Boca Raton, FL: CRC Press.
26. Tozluoğlu M, Tournier AL, Jenkins RP, Hooper S, Bates PA, Sahai E. 2013 Matrix geometry determines optimal cancer cell migration strategy and modulates response to interventions. *Nat. Cell Biol.* **15**, 751–762. (doi:10.1038/ncb2775)
27. Garcia S, Hannezo E, Elgeti J, Joanny J-F, Silberzan P, Gov NS. 2015 Physics of active jamming during collective cellular motion in a monolayer. *Proc. Natl Acad. Sci. USA* **112**, 15 314–15 319. (doi:10.1073/pnas.1510973112)
28. Kabla AJ. 2012 Collective cell migration: leadership, invasion and segregation. *J. R. Soc. Interface* **9**, 3268–3278. (doi:10.1098/rsif.2012.0448)
29. Szabó A, Unnep R, Méhes E, Twal WO, Argraves WS, Cao Y, Czirók A. 2010 Collective cell motion in endothelial monolayers. *Phys. Biol.* **7**, 46007. (doi:10.1088/1478-3975/7/4/046007)
30. Lee RM, Kelley DH, Nordstrom KN, Ouellette NT, Losert W. 2013 Quantifying stretching and rearrangement in epithelial sheet migration. *New J. Phys.* **15**, 25036. (doi:10.1088/1367-2630/15/2/025036)
31. Zimmermann J, Hayes RL, Basan M, Onuchic JN, Rappel W-J, Levine H. 2014 Intercellular stress reconstitution from traction force data. *Biophys. J.* **107**, 548–554. (doi:10.1016/j.bpj.2014.06.036)
32. Basan M, Prost J, Joanny J-F, Elgeti J. 2011 Dissipative particle dynamics simulations for biological tissues: rheology and competition. *Phys. Biol.* **8**, 26014. (doi:10.1088/1478-3975/8/2/026014)
33. Zimmermann J, Camley BA, Rappel W-J, Levine H. 2016 Contact inhibition of locomotion determines cell–cell and cell–substrate forces in tissues. *Proc. Natl Acad. Sci. USA* **113**, 2660–2665. (doi:10.1073/pnas.1522330113)
34. Lee RM, Yue H, Rappel W-J, Losert W. 2017 Data from: Inferring single cell behavior from large-scale epithelial sheet migration patterns. Digital Repository at the University of Maryland (DRUM). (doi:10.13016/M2855R)
35. Adrian RJ, Westerweel J. 2010 *Particle image velocimetry*. Cambridge, UK: Cambridge University Press.
36. Henkes S, Fily Y, Marchetti MC. 2011 Active jamming: self-propelled soft particles at high density. *Phys. Rev. E* **84**, 040301. (doi:10.1103/PhysRevE.84.040301)
37. Mayor R, Etienne-Manneville S. 2016 The front and rear of collective cell migration. *Nat. Rev. Mol. Cell Biol.* **17**, 97–109. (doi:10.1038/nrm.2015.14)
38. Gov NS. 2007 Collective cell migration patterns: follow the leader. *Proc. Natl Acad. Sci. USA* **104**, 15 970–15 971. (doi:10.1073/pnas.0708037104)
39. Poujade M, Grasland-Mongrain E, Hertzog A, Jouanneau J, Chavrier P, Ladoux B, Buguin A, Silberzan P. 2007 Collective migration of an epithelial monolayer in response to a model wound. *Proc. Natl Acad. Sci. USA* **104**, 15 988–15 993. (doi:10.1073/pnas.0705062104)
40. Khalil A, Friedl P. 2010 Determinants of leader cells in collective cell migration. *Integr. Biol.* **2**, 568–574. (doi:10.1039/c0ib00052c)
41. Farooqui R, Fenteany G. 2005 Multiple rows of cells behind an epithelial wound edge extend cryptic lamellipodia to collectively drive cell-sheet movement. *J. Cell Sci.* **118**, 51–63. (doi:10.1242/jcs.01577)
42. Goehring NW, Grill SW. 2013 Cell polarity: mechanochemical patterning. *Trends Cell Biol.* **23**, 72–80. (doi:10.1016/j.tcb.2012.10.009)
43. Tarle V, Ravasio A, Hakim V, Gov NS. 2015 Modeling the finger instability in an expanding cell monolayer. *Integr. Biol.* **7**, 1218–1227. (doi:10.1039/C5IB00092 K)
44. Zaritsky A, Kaplan D, Hecht I, Natan S, Wolf L, Gov NS, Ben-Jacob E, Tsarfaty I, Asthagiri AR. 2014 Propagating waves of directionality and coordination orchestrate collective cell migration. *PLoS Comput. Biol.* **10**, e1003747. (doi:10.1371/journal.pcbi.1003747)